Reexamining the Mechanical Property Space of
Three-Dimensional Lattice Architectures

Lucas R. Meza[1]*, Greg Phlipot[1], Carlos M. Portela[1], Alessandro Maggi[1], Lauren C. Montemayor[1†], Andre Comella[1], Dennis M. Kochmann[1,2], Julia R. Greer[1]

1. Division of Engineering and Applied Science, California Institute of Technology, Pasadena CA, 91125
2. Department of Mechanical and Process Engineering, ETH Zürich, 8093 Zürich, Switzerland
† Currently at NASA Jet Propulsion Laboratory, Pasadena CA, 91109
*Corresponding Author: lmeza@caltech.edu

Abstract

Lightweight materials that are simultaneously strong and stiff are desirable for a range of applications from transportation to energy storage to defense. Micro- and nanolattices represent some of the lightest fabricated materials to date, but studies of their mechanical properties have produced inconsistent results that are not well captured by existing lattice models. We performed systematic nanomechanical experiments on four distinct geometries of solid polymer and hollow ceramic (Al_2O_3) nanolattices. All samples tested had a nearly identical scaling of strength (σ_y) and Young's modulus (E) with relative density ($\bar{\rho}$), ranging from $\sigma_y \propto \bar{\rho}^{1.45}$ to $\bar{\rho}^{1.92}$ and $E \propto \bar{\rho}^{1.41}$ to $\bar{\rho}^{1.83}$, revealing that changing topology alone does not necessarily have a significant impact on nanolattice mechanical properties. Finite element analysis was performed on solid and hollow lattices with structural parameters beyond those realized experimentally, enabling the identification of transition regimes where solid-beam lattices diverge from existing analytical theories and revealing the complex parameter space of hollow-beam lattices. We propose a simplified analytical model for solid-beam lattices that provides insight into the mechanisms behind their observed stiffness, and we investigate different hollow-beam lattice parameters that give rise to their aberrant properties. These experimental, computational and theoretical results uncover how architecture can be used to access unique lattice mechanical property spaces while demonstrating the practical limits of existing beam-based models in characterizing their behavior.

Keywords: Nanolattices, nanoarchitected materials, lattices, cellular solids, mechanics

1. Introduction

Incorporating three-dimensional architecture into materials design across multiple length scales has led to the creation of advanced materials with novel mechanical properties, such as ultralight weight [1–3], negative Poisson's ratios [4,5], and near infinite bulk-to-shear modulus ratios [6,7]. The versatility of current fabrication methods and processing techniques engenders a virtually unbounded potential design space by which new materials can be created [8–17]. Despite many proof-of-concept demonstrations, very few guiding principles exist for designing architectures that efficiently integrate structural and microstructural deformation mechanisms. Understanding the complex interplay between

constituent materials and architecture is crucial to creating and optimizing new materials with tunable properties.

One of the more prominent recent successes of architected materials has been the creation of simultaneously lightweight, strong and stiff three-dimensional micro- and nanolattices. These materials are 3D assemblies of beams with micro- and nanoscale constituent dimensions, and it is the confluence of nanometer-sized dimensions and architecture that gives rise to their unique properties [1–3,15,18–26]. The theoretical maximum Young's modulus (E) and yield strength (σ_y) of a lightweight porous material are set by the Voigt bound, which are functions of the relative density ($\bar{\rho}$) as $E = E_s\bar{\rho}$ and $\sigma_y = \sigma_{ys}\bar{\rho}$. E_s and σ_{ys} are the constituent material's Young's modulus and yield strength, respectively. This means that if a material is 10% dense, its highest possible stiffness and strength are 10% of those of the fully dense solid. [27]. For isotropic solids, the Young's modulus limit is defined by the Hashin-Shtrikman bound [28], and for isotropic beam-based lattices the modulus limit is defined by the tighter Gurtner-Durand bound [29]. This scaling of stiffness and strength with relative density becomes particularly conspicuous for light and ultralight materials, where poor scaling relations can have orders-of-magnitude effects on the overall mechanical properties.

A large body of theoretical and experimental work has been dedicated to creating new lattice architectures and investigating their properties [1,15,18,19,23,30–34]. Most analytical models for the mechanical behavior of both 2D and 3D lattices are derived using beam theory, and these models generally predict that strength and modulus follow a power law scaling with relative density as

$$E = BE_s\bar{\rho}^m, \tag{1}$$

$$\sigma_y = C\sigma_{ys}\bar{\rho}^n. \tag{2}$$

The proportionality constants B and C and the scaling coefficients m and n change depending on whether lattice deformation is dominated by stretching or bending of the beams. To predict if a lattice will be stretching- or bending-dominated, pin-jointed versions of the lattices have to be analyzed to assess their rigidity. A pin-jointed structure is defined to be *rigid* if any shape change requires a corresponding increase in strain energy [30,35]. Structures can also be periodically rigid if they are constructed from rigid periodic subunits. An in-depth discussion of rigidity can be found in the Supplementary Materials. According to classical formulations, lattices with a rigid topology have properties governed by stretching of the beams, with $E \propto \bar{\rho}$ and $\sigma_y \propto \bar{\rho}$ ($m = n = 1$), and lattices with a non-rigid topology are governed by bending of the beams, with $E \propto \bar{\rho}^2$ and $\sigma_y \propto \bar{\rho}^{1.5}$ ($m = 2, n = 1.5$) [36]. Topology here refers to structures as defined by their connectivity, and it is invariant to changes in structural parameters like beam diameter or shell thickness.

These theories provide a simple framework to predict the mechanical performance of lattices, but their utility as analysis tools for physically realizable systems has yet to be fully quantified. Experimental and theoretical work on lattices have shown mixed results on the exact role of topology in governing strength and modulus scaling; a wide range of reported strength and stiffness power law scaling relationships exists, even for topologically identical systems, and no experimentally realized

lightweight lattice matches the performance predicted by the Gurtner-Durand bound [1,2,18,21–23,37,38].

We conducted systematic nanomechanical experiments and finite element analysis on nanolattices made from two different material systems, with four different topologies each. We found that the mechanical properties of nanolattices in a currently experimentally realizable property space are nearly independent of architecture, and that the strength and stiffness of rigid and non-rigid topologies at the same relative density are nearly identical. This result represents a significant point of departure from theories relating mechanical properties to the rigidity of the lattice topology [39]. Uniaxial compression experiments reveal a non-linear scaling of strength and stiffness with relative density, with exponents between $m = 1.41 - 1.83$ for stiffness and $n = 1.45 - 1.92$ for strength for all nanolattice topologies and material systems. Finite element simulations (Abaqus FEA) reproduce the observed nonlinear scaling within the range of relative densities tested experimentally for both solid and hollow-beam nanolattices. They further reveal that for solid lattices with relative densities of $\bar{\rho} < 5\%$, the stiffnesses of rigid and non-rigid topologies deviate from one another to show good agreement with existing bending- and stretching-dominated scaling laws [39]. For hollow lattices, finite element simulations reveal a highly complex parameter space with orders-of-magnitude deviations in stiffness arising from small variations in parameters. We propose a simple analytic framework that provides insight into the stiffness scaling of solid-beam lattices, and we investigate some of the mechanisms for the large variances in hollow-beam lattice properties.

2. Methods

2.1 Fabrication

Polymer nanolattices were fabricated using a two-photon lithography direct laser writing process in IP-Dip photoresist using the Photonic Professional lithography system (Nanoscribe GmbH). Structures were written using laser powers of $6 - 14\ mW$ and writing speeds of $\sim 50\ \mu m\ s^{-1}$. Laser power is used to control the beam diameters. As a byproduct of the fabrication process, all beams were elliptical, with an aspect ratio of ~3:1. Beams can be made to be circular by writing structures using a layer-by-layer process, but this writing method results in structures with larger dimensions. The smallest beam dimensions that can be written using this process are on the order of ~200nm, and in this work the beam dimensions range from 400nm – 2μm. Unit cell sizes of fabricated nanolattices ranged from 3 to 15μm, and overall sample dimensions were between 25 and 85μm.

Hollow structures were written using the polymer nanolattices as a base scaffold; polymer surfaces were conformally coated in alumina (Al$_2$O$_3$) using atomic layer deposition (ALD). Deposition was done at 150°C in a Cambridge Nanotech S200 ALD system using the following steps: H$_2$O is pulsed for $15\ ms$, the system is purged for $20\ s$, trimethyl aluminum (TMA) is pulsed for $15\ ms$, the system is purged for $20\ s$, and the process is repeated. The carrier gas is nitrogen, flown at a rate of $20\ sccm$ (standard cubic centimeters per minute). The process was cycled for between 50 and 1200 cycles to obtain the desired thickness coatings on the nanolattices, which ranged from 5 to 120nm. The thickness of the coatings was verified using spectroscopic ellipsometry with an alpha-SE Ellipsometer (J.A. Wollam

Co., Inc.). After deposition, two outer edges of the coated nanolattices were removed using focused ion beam (FIB) milling in an FEI Nova 200 Nanolab system to expose the polymer to air. After this exposure, the samples were placed into an O_2 plasma barrel asher for a time period between 50 and 75 hours with a $300\ sccm$ flow rate of O_2 under $100\ W$ of power to fully remove the polymer. This process is nearly identical to that reported in [21].

2.2 Nano-Mechanical Experiments

Monotonic and cyclic uniaxial compression experiments were performed on nanolattices in a G200 XP Nanoindenter (Agilent Technologies). Structures were compressed uniaxially to $\sim 50\%$ strain at a rate of $10^{-3}\ s^{-1}$ to determine their yield stress (σ_y), Young's modulus (E) and overall deformation characteristics. The data obtained from nanolattice compression experiments performed in this work had a wide range of stress-strain responses, which required the formulation of a consistent method to measure meaningful Young's modulus and yield strength. In every sample tested, the stress-strain data was comprised of a toe region, a linear region, and a failure region (Figure S1). The toe region is a non-linear segment of data at the beginning of loading, and generally corresponds to slight misalignments and imperfections between the sample and the indenter tip. For each sample, a subset of stress-strain data was taken starting at the beginning of loading and going to the onset of failure (shown in blue in Figure S1). The maximum slope of this data subset was defined as the Young's modulus, E. This is done to mitigate the effect of the toe region on the stiffness measurement. In polymer samples, or any sample with ductile yielding, a line with slope E is determined using a 0.2% strain offset from the obtained Young's modulus fit, and the intersection of this line and the stress-strain data is taken to be the yield strength σ_y (Figure S1A). In hollow Al_2O_3 samples, or any sample with a brittle yielding, the yield strength is taken to be the peak stress before failure (Figure S1B). It should be noted that edge effects that arise due to the finite sample size can affect the strength and stiffness, particularly for non-rigid topologies, so the strength and stiffness of lattices here is an *effective* structural response that approximates the properties of an infinite lattice.

2.3 Finite Element Modeling

Finite element simulations of the solid and hollow unit cells were performed in the commercial finite element code Abaqus. All simulations were performed statically with linear perturbations to obtain the linear stiffness of each topology. The solid unit cell simulations were performed using C3D10 10-node quadratic tetrahedral elements, and the hollow simulations used S3R 3-node shell elements to represent the discretized unit cells. An isotropic linear elastic material model was used for both solid and hollow structure simulations, and stiffnesses for the constituent polymer and Al_2O_3 were obtained from literature [23,40]. Solid unit cell simulations had between $25,000 - 250,000$ elements and hollow unit cell simulations had between $25,000 - 100,000$ elements; the exact number of elements varied depending on the unit cell and structural parameters used.

Simulations of the full-scale lattices tested in the experiments required prohibitively expensive computational resources, so single unit cells subject to periodic boundary conditions (PBCs) were simulated to obtain the effective stiffness of the periodic lattices. PBCs were manually implemented in a

similar fashion to [41]. To simulate uniaxial stressing of the periodic structure, the *z*-component of the volume-averaged strain was imposed, while the transverse components remained unconstrained and periodicity of the unit cell was enforced by solving for the unknown relative displacements U_i^Δ on the *X*- and *Y*-faces below. The procedure of implementing the PBCs is summarized below.

For each node on X^--face: Find matching node on X^+-face
Constrain transverse displacements: $U_1^+ - U_1^- = U_1^\Delta$
Constrain in-plane displacements: $U_2^+ = U_2^-$, $U_3^+ = U_3^-$
Constrain rotations: $R_i^+ = R_i^-$ (i = 1,2,3)
Repeat for *Y*- and *Z*-faces
Constrain volume-averaged strain in *z*-direction: $U_3^\Delta = \Delta z$

Note that the rotation constraint was only needed for the hollow simulations since the tetrahedron elements used in the solid unit cell simulations do not have rotational degrees of freedom. The effective stiffness of the periodic lattice was calculated as the ratio between the average strain and the average stress of the unit cell in the *z*-direction. Taking F to be the reaction force across the top surface and L to be the unit cell side length, the modulus was calculated as

$$E = \frac{\sigma_{avg}}{\varepsilon_{avg}} = \frac{F}{L\,\Delta z}. \tag{3}$$

3. Theory

The mechanical properties of periodic lattices are commonly modeled using the bending or stretching behavior of the constituent beams [2,5,19,36,37,42]. In classical formulations, beams in a lattice are assumed to be slender and are approximated as Euler-Bernoulli or Timoshenko beams [39,43]. Deformation modes like shearing and torsion in the beams and compression and bending of the nodes are often neglected in these simplified analyses because of the complexity associated with incorporating them into models and their negligible influence in slender beam lattices. In a non-rigid lattice comprised of solid Euler-Bernoulli beams with a characteristic cross-sectional dimension R and length L, the stiffness is assumed to be dominated by bending of the beams, giving rise to a scaling of $E \propto (R/L)^4$ [39,44]. In a rigid lattice, this scaling is $E \propto (R/L)^2$ and arises from the assumption that stiffness is governed by stretching and compression of the beams [19,44]. In lattices with very slender beams (i.e. $\lambda \gtrsim 20$), the relative density can be approximated to scale as $\bar{\rho} \propto (R/L)^2$, where the slenderness is defined as $\lambda = \sqrt{AL^2/I}$, with A being the cross-sectional area and I being the area moment of inertia of the beam. These three relationships give rise to the classical stiffness scaling of $E \propto \bar{\rho}^2$ for "bending-dominated" and $E \propto \bar{\rho}$ for "stretching-dominated" cellular solids.

These simplified relations begin to break down when the beams in a lattice cannot be approximated as slender. Simplified relative density relations are obtained by ignoring the relative contribution of beams intersecting at the nodes. Accounting for the effects of nodal intersections, we derived the relative densities of lattices with solid and hollow circular beams as a function of R/L and t/R to have the functional forms

5

$$\bar{\rho}_{solid} = C_1 \left(\frac{R}{L}\right)^2 + C_2 \left(\frac{R}{L}\right)^3, \tag{4}$$

$$\bar{\rho}_{hollow} = C_1 \left(\frac{R}{L}\right)^2 f\left(\frac{t}{R}\right) + C_2 \left(\frac{R}{L}\right)^3 g\left(\frac{t}{R}\right), \tag{5}$$

where C_1 and C_2 are geometry-dependent constants and are equal in solid and hollow lattices with the same geometry. $f\left(\frac{t}{R}\right) = 2\left(\frac{t}{R}\right) - \left(\frac{t}{R}\right)^2$ is the hollow-cylinder correction, and $g\left(\frac{t}{R}\right) = 3\left(\frac{t}{R}\right) - 3\left(\frac{t}{R}\right)^2 - \left(\frac{t}{R}\right)^3$ is the hollow-sphere correction. This model accurately predicts relative density scaling over a wide range of beam slendernesses, and notably diverges from models that do not account for nodal corrections in solid and hollow lattices when beam slenderness is $\lambda < 20$ (Figure S2). A full derivation of this equation for an octahedron lattice is provided in the Supplementary Materials.

Classical stiffness models ignore the combined influence of stretching and bending in beams by assuming that one has a dominant effect over the other. In real lattices, this assumption no longer holds, and beams in a non-slender lattice are subject to both bending and stretching, in addition to other effects such as shearing, torsion and nodal interactions. To account for some of these effects, we developed a simple analytical model that accurately captures the stiffness of rigid and non-rigid lattices by representing them as 3D networks of solid Euler-Bernoulli beams subject to bending and axial compression and tension. In this framework, the Young's modulus of *non-rigid* and *rigid* lattices scales as

$$E_{non-rigid} = \frac{E_s}{A_1 \left(\frac{R}{L}\right)^{-2} + A_2 \left(\frac{R}{L}\right)^{-4}}, \tag{6}$$

$$E_{rigid} = \frac{E_s \left(1 + B_3 \left(\frac{R}{L}\right)^{-2}\right)}{B_1 \left(\frac{R}{L}\right)^{-2} + B_2 \left(\frac{R}{L}\right)^{-4}}. \tag{7}$$

Here, A_1, A_2, B_1, B_2, and B_3 are geometry-dependent constants, and E_s is the modulus of the constituent solid material (a full derivation of Eqs. (6 and (7 is provided in the Supplementary Materials). Similar equations can be derived for hollow beam lattices. This model predicts an inherently non-power law scaling between stiffness and relative density in rigid and non-rigid lattices. In the limit of very slender beams, i.e. $R/L \ll 1$, Eqs. (6 and (7 approach the simplified models for bending- and stretching-dominated solids [19,39], but for lattices with less slender beams, i.e. $R/L \gtrsim 0.05$, the relative influence of the bending and stretching terms are comparable, and the stiffness transitions to an intermediate scaling that falls between the reduced quadratic stretching and quartic bending scaling relationships (Figure S4).

4. Results

We fabricated four nanolattice topologies with varying degrees of rigidity and average nodal connectivity (Z): (1) an octet-truss (rigid, $Z = 12$), (2) a cuboctahedron (periodically rigid, $Z = 8$), (3) a

3D Kagome (periodically rigid, $Z = 6$), and (4) a tetrakaidecahedron (non-rigid, $Z = 4$) (Figure 1). Each nanolattice was constructed out of solid polymer and hollow Al_2O_3 beams with elliptical cross sections, which arise as a result of the fabrication method [21,23]. Octet-truss, cuboctahedron and tetrakaidecahedron samples were made with 5x5x5 unit cells, and 3D Kagome samples were made with 6x6x3 unit cells. The relative densities of fabricated samples ranged from $\bar{\rho} = 1.1\% - 62.6\%$ for solid polymer and $\bar{\rho} = 0.14\% - 9.1\%$ for hollow Al_2O_3 and spanned at least one order of magnitude within each topology. The slenderness of the beams ranged from $\lambda = 13.8 - 62.8$ for polymer samples and $\lambda = 12.0 - 59.8$ for Al_2O_3 samples. Despite the high relative density of some of the samples, each individual architecture remained topologically identical throughout its relative density range, and most samples had $\bar{\rho} \leq 30\%$.

We experimentally investigated strength and stiffness scaling relations of the nanolattices across all topologies, dimensions, and material systems and found that in the monolithic polymer samples the scaling exponents for stiffness range from $m = 1.41 - 1.83$ and those for strength range from $n = 1.63 - 1.92$. In the hollow Al_2O_3 samples, the stiffness exponents range from $m = 1.46 - 1.73$ and the strength exponents range from $n = 1.45 - 1.77$. Table 1 provides the scaling and proportionality constants for all topologies and material systems explored in this work, and coefficients of determination (R^2) for these fits can be found in the Supplementary Materials (Table S2). The plots of strength and stiffness vs. density in Figure 2 show that the mechanical properties of all topologies at the same density effectively collapse onto each other for each material system. Little variation exists in the proportionality constants or scaling exponents for Young's modulus between the two material systems, and the strength proportionality constants and scaling exponents of the polymer nanolattices are slightly higher than those of the Al_2O_3 nanolattices. These results demonstrate that in the range of relative densities tested for both materials systems, virtually no correlation exists between the rigidity of the samples and their strength and stiffness scaling. This finding is surprising because it indicates that topology has a less significant role in controlling the strength and stiffness of lattices than commonly theorized [19,36,39].

Finite element (FE) simulations of monolithic polymer lattices help shed light onto the underlying causal mechanisms for this observed deviation from analytical predictions. Figure 3 shows that at the relative densities investigated in the experiments, the simulated stiffnesses are in excellent agreement with the experimental results and show a similar nonlinear scaling. At relative densities below experimentally attainable ones, the simulations show a transition to a different, topology-dependent scaling relation. For the rigid octet-truss and periodically rigid cuboctahedron, we identified a transition in the stiffness scaling from $m \approx 2$ when the beams have slendernesses of $\lambda < 25$ ($\bar{\rho} \gtrsim 10\%$) to $m \approx 1$ when the beams have slendernesses of $\lambda > 25$ ($\bar{\rho} \lesssim 10\%$). Similarly, a transition from $m \approx 1.4$ when beams have slendernesses of $\lambda < 27$ ($\bar{\rho} \gtrsim 9\%$) to $m \approx 1$ when beams have slendernesses of $\lambda > 27$ ($\bar{\rho} \lesssim 9\%$) exists for the periodically rigid 3D Kagome. For the non-rigid tetrakaidecahedron, a similar transition occurs from a scaling of $m \approx 1.5$ when the beams have slendernesses of $\lambda < 7$ ($\bar{\rho} \gtrsim 7\%$) to $m \approx 2$ when the beams have slendernesses of $\lambda > 7$ ($\bar{\rho} \lesssim 7\%$), which matches the analytic prediction for a non-rigid topology of $E \propto \bar{\rho}^2$. The stiffnesses of various nanolattice topologies at these low relative densities are also well predicted by Timoshenko and Euler-Bernoulli beam models in all

cases except for the 3D Kagome lattice (Figure S4), a point that is examined in more detail in the Discussion section. The FE scaling fits shown in Figure 3 are taken using the 4 densest and 4 least dense points, which is the reason for the slight discrepancy from the experimentally obtained scaling coefficients.

Finite element simulations of hollow Al_2O_3 nanolattices with the same structural parameters as used in experiments corroborated most of the experimental findings. Simulations for octet, cuboctahedron and 3D Kagome lattices match experimental results at high relative densities ($\bar{\rho} \gtrsim 1\%$) and are at most a factor of 2-3 higher than experimental results at the lowest relative densities ($\bar{\rho} \lesssim 1\%$) (Figure 4A and B). The simulated tetrakaidecahedron stiffness matches experimental results across the entire range of relative densities (Figure 4C). Simulations of hollow nanolattices with structural parameters that span beyond those that were tested experimentally reveal a more complex landscape. A highly non-linear relationship between Young's modulus and relative density emerges in hollow octet-truss simulations when the beam wall thickness-to-length ratio (t/L) is held constant and the beam semi-minor axis-to-length ratio (R/L) is varied, with large deviations from experimental stiffness scaling (Figure 5A). We observed a similar deviation from linearity in the hollow tetrakaidecahedron, but the result is less pronounced (Figure 5B). We also found that Timoshenko and Euler-Bernoulli beam models consistently overpredict the stiffnesses of hollow nanolattice topologies across all relative densities (Figure S5).

5. Discussion

5.1. Solid Beam Nanolattices

The strong agreement between FE and experimental results for solid nanolattices across all relative densities and topologies suggests that the FE models accurately capture the dominant features that govern the elastic behavior (Figure 3). The small variance between the two results can be attributed to factors like waviness in the beams [23], non-uniformity of the cross sections [45], surface roughness [23], misalignment of the nodes, and edge effects from the finite size of the samples in experiments. Some of these factors are investigated further in the Supplementary Materials; our results suggest that they do not play a dominant role in the stiffness of solid beam lattices studied in this work. These results are also generalizable to lattices of arbitrary dimension, and additional experiments performed on macroscopic octet-truss polymer lattices demonstrated a similar scaling to that seen for the nanolattices (Figure S11). Solid-beam nanolattices in low-density regimes are difficult to realize experimentally because of their high sensitivity to defects and external processing parameters. All nanolattices with beams that had slendernesses of $\lambda > 70$ were prone to spontaneous collapse because small stresses that arise during writing and developing of the photopolymer can cause premature buckling of the highly slender beams. This is what set the relative density limit of the solid polymer samples in this work.

The close agreement between the FE, Euler-Bernoulli and Timoshenko beam results at low densities ($\bar{\rho} < 1\%$) suggests that beam theories are adequate to predict lattice stiffnesses in these regimes (Figure S4). At higher relative densities, Euler-Bernoulli beam lattice simulations show a divergence from power law scaling that is similar to experimental data and FE results and generally

underpredict the magnitude of the stiffness (Figures S4). Simulations using Timoshenko beam models, which account for shear deformation and are used to model less slender beams, have a lower stiffness than Euler-Bernoulli beam models and further underpredict the stiffness. The simplified stiffness model in Eq. (6 provides insights into the mechanisms for the scaling of rigid and non-rigid solid beam lattices, viz. that there are contributions from both bending and stretching of beams at high relative densities, which leads to a stiffening behavior, but it does not fully capture the mechanisms behind the observed deviation. The incorrect stiffness prediction of beam-based models occurs primarily because they fail to account for the contribution of the nodes to the overall mechanical properties. In solid-beam lattices, the nodes form solid joints that hinder beam rotation, shortening the effective length of the constituent beams and generally leading to higher stiffnesses. While beam models that capture shearing behavior, such as Timoshenko models, can be used to more accurately capture the behavior of short beams [20,46], they lead to a drop in the effective stiffness, which is opposite from the trend observed here. Accurately replicating the mechanics of solid lattices with computationally efficient models, similar to what is done using beam elements, requires in-depth investigations into the role of nodes on the mechanical properties, which is outside the scope of this work.

At the lowest simulated relative densities ($\bar{\rho} \leq 1\%$), the FE results show that Young's modulus of monolithic polymer cuboctahedron and octet-truss lattices scales as $E = E_s\bar{\rho}/8.7$ and $E = E_s\bar{\rho}/9.0$, respectively (Figure 3A&B). These moduli agree well with the existing analytic prediction for the modulus of $E = \bar{\rho}E_s/9$ using pin-jointed bars [19], and are well matched by Euler-Bernoulli and Timoshenko beam models. For the 3D Kagome lattices, FE results predict a stiffness scaling of $E = E_s\bar{\rho}/6$ at low relative densities (Figure 3C). This result is different than both the Euler-Bernoulli and Timoshenko beam simulations (Figure S4). This difference occurs because the 3D Kagome lattice is periodically rigid and has a low connectivity, making it highly sensitive to imperfections and boundary conditions. The FE simulations were performed using periodic boundary conditions, making the lattice effectively infinite; the Euler-Bernoulli simulations were performed on a finite lattice, rendering them sensitive to boundary conditions and preventing them from attaining a linear scaling at low relative densities. This suggests that it is impossible in a practical sense to fabricate a 3D Kagome lattice with a perfectly linear stiffness scaling at any relative density.

5.2. Hollow Beam Nanolattices

The mechanical behavior of hollow-beam nanolattices is notably different from that of solid-beam nanolattices. Two main factors affect the stiffness of hollow lattices: (1) the hollow nodes in thin-walled beams become highly compliant in bending and lead to a reduced overall stiffness, and (2) the surface roughness that arises from beam waviness inherent in the manufacturing process can cause a significant drop in both axial and bending stiffness at low wall thicknesses (Table S3 and [23]). Euler-Bernoulli and Timoshenko beam simulations for hollow lattices fail to capture the effect of the hollow nodes and, as a result, consistently overpredict the stiffness (Figure S5).

Fully resolved finite element simulations of the hollow lattices capture the effect of the nodes, and because they are performed on ideal structures, the observed discrepancy from experiments can primarily be attributed to the imperfections. Octet-truss, cuboctahedron and 3D Kagome lattices

transmit load relatively uniformly throughout their beams (Figure 4A-C), rendering their thinner-walled variations highly sensitive to roughness. This thin-walled sensitivity correlates well with the observed overprediction of the stiffness in the FE simulations at low relative densities (Figure 4). The non-rigid tetrakaidecahedron lattices accommodate macroscopic deformation through local deformation at the nodes (Figure 4D), which causes them to be sensitive to nodal compliance and less sensitive to the beam waviness. The primary imperfections at the nodes exist in the form of misalignment [15], which have a minimal effect on the stiffness [20] and lead to an agreement between FE and experimental results across the tested range of relative densities. The effect of beam waviness has been quantified in the Supplementary Materials.

The complex parameter space revealed by FE simulations of hollow nanolattices (Figure 5) arises because the relative density and stiffness depend on two dimensionless parameters: R/L and t/L, where R is the minor axis of the elliptical beam, t is the wall thickness, and L is the length of the beam. The highly non-linear relationship between relative density and these dimensionless parameters (Eq. (5)) can give rise to hollow nanolattices with different R/L and t/L that have identical relative density (Figure S2B). This leads to situations where samples can have the same geometry, wall thickness, and relative density but can have over an order-of-magnitude difference in stiffness. For example, simulations of two different hollow octet unit cells with the same wall-thickness-to-length ratio, $t/L = 10^{-3}$, and with two different cross-sectional dimensions of $R/L = 0.1$ ($\bar{\rho} = 0.78\%$) and $R/L = 0.15$ ($\bar{\rho} = 0.81\%$), have stiffnesses of 11 MPa and 205 MPa, respectively. These samples are visually distinct (Figure 5A), with one appearing more similar to a solid beam lattice and the other more closely resembling a membrane structure, but they are topologically identical. This complex parameter space reveals that classical scaling laws that depend only on architecture and relative density are incapable of fully capturing the mechanical properties of hollow lattices, and new theories that incorporate the effect of hollow nodes are needed to accurately predict their stiffness. It should be noted that the ellipticity of the beams will have an effect on the stiffness of the lattices, particularly for low-slenderness beams, but quantifying this effect is beyond the scope of this manuscript.

5.3. Strength

The scaling relationships between strength and relative density observed experimentally for almost all nanolattice topologies from both material systems have lower scaling exponents than what is predicted analytically for a bending-dominated solid ($\sigma_y \propto \bar{\rho}^{1.5}$). This implies that additional deformation and failure mechanisms exist that have a greater impact on the strength than do stress concentrations that arise from pure bending. For example, it has been observed that buckling can have a significant impact on the strength of a lattice with the strength-density relation of $\sigma_y \propto \bar{\rho}^{2.5}$ [47]. In polymer and hollow nanolattices, we observed failure initiation at or near the nodes in most samples, which suggests that the nodes govern the strength scaling, similar to what has been observed in microlattices [32]. All the beams in lattice architectures terminate at the nodes at a sharp angle, which creates significant stress concentrations in these locations during deformation. The fixed boundary of a node for a beam in bending represents the location of highest moment and stress, which creates an

additional stress concentration. Fully investigating the effect of stress concentrations near nodes on the strength and stiffness scaling of lattices merits an independent research pursuit.

5.4 Additional Factors Affecting Stiffness and Strength

We have experimentally investigated other factors in some detail that are known to affect the stiffness and strength of lattices: changing the angle of beams, removing beams, and misaligning nodes. The effect of changing lattice angles, which in this case introduces structural anisotropy, was studied using hollow 3D Kagome lattices. Our results show that the stiffness and strength of a lattice at a given relative density change with angle θ approximately as $\sin^4(\theta)$ and $\sin^2(\theta)$, which is in good agreement with previously theorized results [48]. We studied the effect of removing beams and misaligning nodes using solid octet-truss lattices. Removing beams simulates the type of imperfection that arises in highly slender lattices when beams are not properly connected at nodes. The strength and stiffness of lattices with removed beams decreased as $E \propto \bar{\rho}^{3.1-4.3}$ and $\sigma_y \propto \bar{\rho}^{3.0-3.8}$ depending on the regions from which they were removed. This degradation in mechanical properties is greater than what is observed even in stochastic materials, suggesting that it can have a hugely detrimental role on lattice stiffness. Nodal misalignment is the most common form of imperfection in lattices fabricated here [20]. In lattices with offset nodes, no observable change in the stiffness occurred, with only a minimal change in the yield strength, which had a ~22% decrease in strength for the most heavily distorted lattice. This means that for any offset in the nodes there will be little detriment to the mechanical properties. These results are discussed at length in the Supplementary Materials.

6. Conclusion

We provide an in-depth exploration of the parameter space of solid- and hollow-beam nanolattices using experiments, finite element analysis, and beam-based numerical simulations and models. Our work establishes that the strength and stiffness of solid- and hollow-beam nanolattices does not correlate with topology alone, but is instead governed by an intricate combination of geometry and structural parameters. Nanolattices with widely different topologies can have nearly identical strength and stiffness at the same relative density, and hollow nanolattices with the same topology and relative density can have widely different stiffness. We postulate that the convergence of strength and stiffness in solid lattices at higher densities is caused by the increased influence of beam intersections at the nodes. The strength and stiffness parameter space of hollow lattices is highly complex and dependent upon changes in beam length, radius and wall thickness, and a detailed study of these parameters must be conducted before their relative influence can be quantified. These results suggest that the existing classification of nanolattice topologies as stretching- or bending-dominated is insufficient, and new theories must be developed to accurately capture the effect of both nodal interferences in solid-beam lattices and empty nodes in hollow-beam lattices on the mechanical properties.

Acknowledgements

References

[1]   T.A. Schaedler, A.J. Jacobsen, A. Torrents, A.E. Sorensen, J. Lian, J.R. Greer, L. Valdevit, W.B. Carter, Ultralight Metallic Microlattices, Science (80-.). 334 (2011) 962–965. doi:10.1126/science.1211649.

[2]   X. Zheng, H. Lee, T.H. Weisgraber, M. Shusteff, J. DeOtte, E.B. Duoss, J.D. Kuntz, M.M. Biener, Q. Ge, J. a. Jackson, S.O. Kucheyev, N.X. Fang, C.M. Spadaccini, Ultralight, ultrastiff mechanical metamaterials, Science (80-.). 344 (2014) 1373–1377. doi:10.1126/science.1252291.

[3]   S.C. Han, J.W. Lee, K. Kang, A New Type of Low Density Material: Shellular, Adv. Mater. 27 (2015) 5506–5511. doi:10.1002/adma.201501546.

[4]   T. Bückmann, N. Stenger, M. Kadic, J. Kaschke, A. Frölich, T. Kennerknecht, C. Eberl, M. Thiel, M. Wegener, Tailored 3D mechanical metamaterials made by dip-in direct-laser-writing optical lithography., Adv. Mater. 24 (2012) 2710–4. doi:10.1002/adma.201200584.

[5]   S. Krödel, T. Delpero, A. Bergamini, P. Ermanni, D.M. Kochmann, 3D Auxetic Microlattices with Independently Controllable Acoustic Band Gaps and Quasi-Static Elastic Moduli, Adv. Eng. Mater. (2013) 1–17. doi:10.1002/adem.201300264.

[6]   M. Kadic, T. Bückmann, N. Stenger, M. Thiel, M. Wegener, On the practicability of pentamode mechanical metamaterials, Appl. Phys. Lett. 100 (2012) 191901. doi:10.1063/1.4709436.

[7]   T. Bückmann, M. Thiel, M. Kadic, R. Schittny, M. Wegener, An elasto-mechanical unfeelability cloak made of pentamode metamaterials., Nat. Commun. 5 (2014) 4130. doi:10.1038/ncomms5130.

[8]   A.J. Jacobsen, W. Barvosa-Carter, S. Nutt, Micro-scale Truss Structures formed from Self-Propagating Photopolymer Waveguides, Adv. Mater. 19 (2007) 3892–3896. doi:10.1002/adma.200700797.

[9]   C. Sun, N. Fang, D.M. Wu, X. Zhang, Projection micro-stereolithography using digital micro-mirror dynamic mask, Sensors Actuators, A Phys. 121 (2005) 113–120. doi:10.1016/j.sna.2004.12.011.

[10]   M. Campbell, D. Sharp, M. Harrison, R. Denning, A. Turberfield, Fabrication of photonic crystals for the visible spectrum by holographic lithography, Nature. 404 (2000) 53–6. doi:10.1038/35003523.

[11]   H.-B. Sun, S. Matsuo, H. Misawa, Three-dimensional photonic crystal structures achieved with two-photon-absorption photopolymerization of resin, Appl. Phys. Lett. 74 (1999) 786–788. doi:DOI:10.1063/1.123367.

[12]   N. Tétreault, G. von Freymann, M. Deubel, M. Hermatschweiler, F. Pérez-Willard, S. John, M. Wegener, G. a. Ozin, New Route to Three-Dimensional Photonic Bandgap Materials: Silicon Double Inversion of Polymer Templates, Adv. Mater. 18 (2006) 457–460. doi:10.1002/adma.200501674.

[13]   J.J. Do Rosário, E.T. Lilleodden, M. Waleczek, R. Kubrin, A.Y. Petrov, P.N. Dyachenko, J.E.C. Sabisch, K. Nielsch, N. Huber, M. Eich, G.A. Schneider, Self-Assembled Ultra High Strength, Ultra Stiff Mechanical Metamaterials Based on Inverse Opals, Adv. Eng. Mater. 17 (2015) 1420–1424. doi:10.1002/adem.201500118.

[14] X. Chen, L. Wang, Y. Wen, Y. Zhang, J. Wang, Y. Song, L. Jiang, D. Zhu, Fabrication of closed-cell polyimide inverse opal photonic crystals with excellent mechanical properties and thermal stability, J. Mater. Chem. 18 (2008) 2262. doi:10.1039/b801565a.

[15] D. Jang, L.R. Meza, F. Greer, J.R. Greer, Fabrication and deformation of three-dimensional hollow ceramic nanostructures, Nat. Mater. 12 (2013) 893–898. doi:10.1038/nmat3738.

[16] N. Kröger, Prescribing diatom morphology: toward genetic engineering of biological nanomaterials., Curr. Opin. Chem. Biol. 11 (2007) 662–9. doi:10.1016/j.cbpa.2007.10.009.

[17] K. Sandhage, M. Dickerson, Novel, Bioclastic Route to Self-Assembled, 3D, Chemically Tailored Meso/Nanostructures: Shape-Preserving Reactive Conversion of Biosilica (Diatom) Microshells, Adv. Mater. 14 (2002) 429–433. http://onlinelibrary.wiley.com/doi/10.1002/1521-4095(20020318)14:6%3C429::AID-ADMA429%3E3.0.CO;2-C/abstract (accessed April 11, 2013).

[18] J. Bauer, A. Schroer, R. Schwaiger, O. Kraft, Approaching theoretical strength in glassy carbon nanolattices, Nat. Mater. 8 (2016). doi:10.1038/NMAT4561.

[19] V.S. Deshpande, N.A. Fleck, M.F. Ashby, Effective properties of the octet-truss lattice material, J. Mech. Phys. Solids. 49 (2001) 1747–1769. doi:10.1016/S0022-5096(01)00010-2.

[20] L.R. Meza, J.R. Greer, Mechanical characterization of hollow ceramic nanolattices, J. Mater. Sci. 49 (2013) 2496–2508. doi:10.1007/s10853-013-7945-x.

[21] L.R. Meza, S. Das, J.R. Greer, Strong, lightweight, and recoverable three-dimensional ceramic nanolattices, Science (80-.). 345 (2014) 1322–1326. doi:10.1126/science.1255908.

[22] X. Zheng, W. Smith, J. Jackson, B. Moran, H. Cui, D. Chen, J. Ye, N. Fang, N. Rodriguez, T. Weisgraber, C.M. Spadaccini, Multiscale metallic metamaterials, Nat. Mater. (2016) 1–8. doi:10.1038/nmat4694.

[23] L.R. Meza, A.J. Zelhofer, N. Clarke, A.J. Mateos, D.M. Kochmann, J.R. Greer, Resilient 3D hierarchical architected metamaterials, Proc. Natl. Acad. Sci. 112 (2015) 11502–11507. doi:10.1073/pnas.1509120112.

[24] B.D. Nguyen, J.S. Cho, K. Kang, Optimal design of "Shellular", a micro-architectured material with ultralow density, Mater. Des. 95 (2016) 490–500. doi:10.1016/j.matdes.2016.01.126.

[25] D. Rayneau-Kirkhope, Y. Mao, R. Farr, J. Segal, Hierarchical space frames for high mechanical efficiency: Fabrication and mechanical testing, Mech. Res. Commun. 46 (2012) 41–46. doi:10.1016/j.mechrescom.2012.06.011.

[26] X. Wendy Gu, J.R. Greer, Ultra-strong architected Cu meso-lattices, Extrem. Mech. Lett. 2 (2015) 7–14. doi:10.1016/j.eml.2015.01.006.

[27] M.A. Meyers, K.K. Chawla, Mechanical Behavior of Materials, 1st ed., Prentice-Hall, Inc., New Jersey, 1998.

[28] Z. Hashin, S. Shtrikman, A variational approach to the theory of the elastic behaviour of multiphase materials, J. Mech. Phys. Solids. 11 (1963) 127–140. doi:10.1016/0022-5096(63)90060-7.

[29] G. Gurtner, M. Durand, Stiffest elastic networks, Proc. R. Soc. A Math. Phys. Eng. Sci. 470 (2014) 20130611–20130611. doi:10.1098/rspa.2013.0611.

[30] V.S. Deshpande, M.F. Ashby, N.A. Fleck, Foam topology: bending versus stretching dominated architectures, Acta Mater. 49 (2001) 1035–1040. doi:10.1016/S1359-6454(00)00379-7.

[31] H.N.G. Wadley, Multifunctional periodic cellular metals, Philos. Trans. R. Soc. A. 364 (2006) 31–68. doi:10.1098/rsta.2005.1697.

[32]   L. Valdevit, S.W. Godfrey, T. a. Schaedler, A.J. Jacobsen, W.B. Carter, Compressive strength of hollow microlattices: Experimental characterization, modeling, and optimal design, J. Mater. Res. 28 (2013) 2461–2473. doi:10.1557/jmr.2013.160.

[33]   K.J. Maloney, C.S. Roper, A.J. Jacobsen, W.B. Carter, L. Valdevit, T.A. Schaedler, Microlattices as architected thin films: Analysis of mechanical properties and high strain elastic recovery, APL Mater. 1 (2013) 22106. doi:10.1063/1.4818168.

[34]   A.J. Jacobsen, S. Mahoney, W.B. Carter, S. Nutt, Vitreous carbon micro-lattice structures, Carbon N. Y. 49 (2011) 1025–1032. doi:10.1016/j.carbon.2010.10.059.

[35]   S. Pellegrino, C.R. Calladine, Matrix Analysis of Statically and Kinematically Indeterminate Frameworks, Int. J. Solids Struct. 22 (1986) 409–428.

[36]   N.A. Fleck, V.S. Deshpande, M.F. Ashby, Micro-architectured materials: past, present and future, Proc. R. Soc. A Math. Phys. Eng. Sci. 466 (2010) 2495–2516. doi:10.1098/rspa.2010.0215.

[37]   T. George, V.S. Deshpande, H.N.G. Wadley, Mechanical response of carbon fiber composite sandwich panels with pyramidal truss cores, Compos. Part A Appl. Sci. Manuf. 47 (2013) 31–40. doi:10.1016/j.compositesa.2012.11.011.

[38]   T. Tancogne-Dejean, A.B. Spierings, D. Mohr, Additively-manufactured metallic micro-lattice materials for high specific energy absorption under static and dynamic loading, Acta Mater. 116 (2016) 14–28. doi:10.1016/j.actamat.2016.05.054.

[39]   L.J. Gibson, M.F. Ashby, Cellular Solids: Structure and Properties, 2nd ed., Cambridge University Press, Cambridge, 1999.

[40]   M. Berdova, T. Ylitalo, I. Kassamakov, J. Heino, P.T. Törmä, L. Kilpi, H. Ronkainen, J. Koskinen, E. Hæggström, S. Franssila, Mechanical assessment of suspended ALD thin films by bulge and shaft-loading techniques, Acta Mater. 66 (2014) 370–377. doi:10.1016/j.actamat.2013.11.024.

[41]   W. Wu, J. Owino, Applying Periodic Boundary Conditions in Finite Element Analysis, Simulia Community Conf. (2014) 707–719.

[42]   J. Bauer, S. Hengsbach, I. Tesari, R. Schwaiger, O. Kraft, High-strength cellular ceramic composites with 3D microarchitecture, Proc. Natl. Acad. Sci. 111 (2014) 2453–2458. doi:10.1073/pnas.1315147111.

[43]   W.Y. Jang, S. Kyriakides, A.M. Kraynik, On the compressive strength of open-cell metal foams with Kelvin and random cell structures, Int. J. Solids Struct. 47 (2010) 2872–2883. doi:10.1016/j.ijsolstr.2010.06.014.

[44]   M.F. Ashby, The properties of foams and lattices., Philos. Trans. A. Math. Phys. Eng. Sci. 364 (2006) 15–30. doi:10.1098/rsta.2005.1678.

[45]   N. Silvestre, Buckling behaviour of elliptical cylindrical shells and tubes under compression, Int. J. Solids Struct. 45 (2008) 4427–4447. doi:10.1016/j.ijsolstr.2008.03.019.

[46]   K.H. Law, L. Gardner, Lateral instability of elliptical hollow section beams, Eng. Struct. 37 (2012) 152–166. doi:10.1016/j.engstruct.2011.12.008.

[47]   A. Torrents, T.A. Schaedler, A.J. Jacobsen, W.B. Carter, L. Valdevit, Characterization of nickel-based microlattice materials with structural hierarchy from the nanometer to the millimeter scale, Acta Mater. 60 (2012) 3511–3523. doi:10.1016/j.actamat.2012.03.007.

[48]   V. Deshpande, Collapse of truss core sandwich beams in 3-point bending, Int. J. Solids Struct. 38 (2001)

Figures
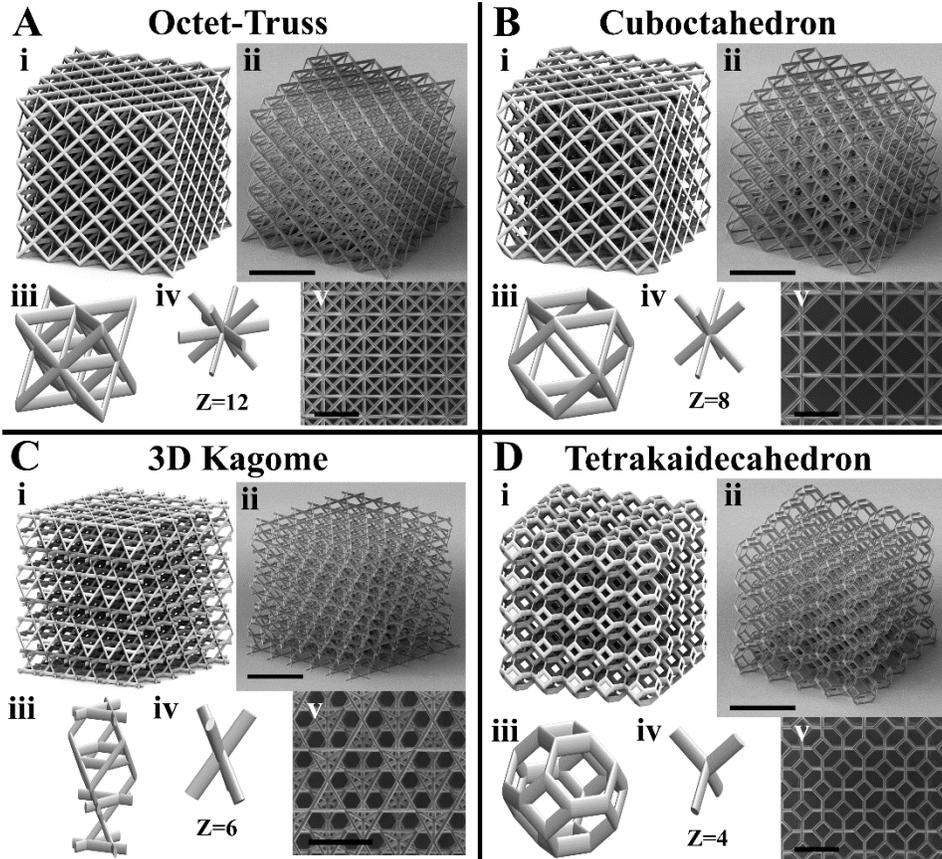
Figure 1: Rigid and non-rigid nanolattice topologies.
The four nanolattice topologies tested in this work: A) octet-truss, B) cuboctahedron, C) 3D Kagome, and D) tetrakaidecahedron. Figures i) are CAD models of the full structures, ii) are SEM images of the full structures, iii) are CAD models of the unit cells, iv) are representative nodes showing the average nodal connectivity, and v) are SEM images from the top of the structures. The scales bars in ii) are 10μm, and the scale bars in v) are 5 μm.
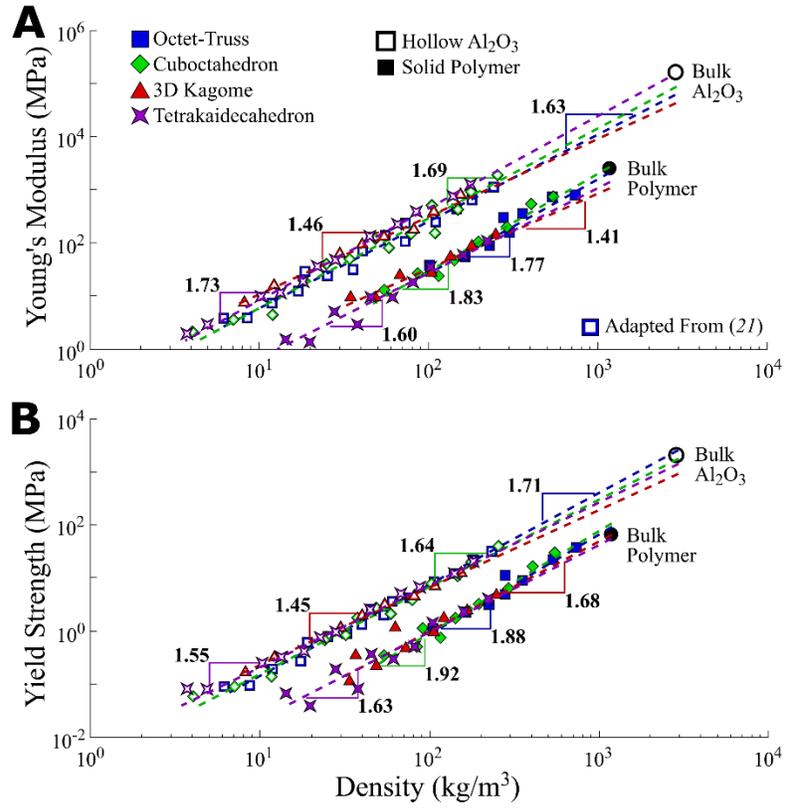
Figure 2: Strength and stiffness vs. density of different nanolattice topologies.
Logarithmic plots of A) Young's modulus vs. relative density and B) yield strength vs. relative density of every sample tested from all four regular topologies and both material systems. The values of the fully dense constituent materials are also plotted. Trend lines for each set of samples are meant to graphically illustrate the scaling relations.
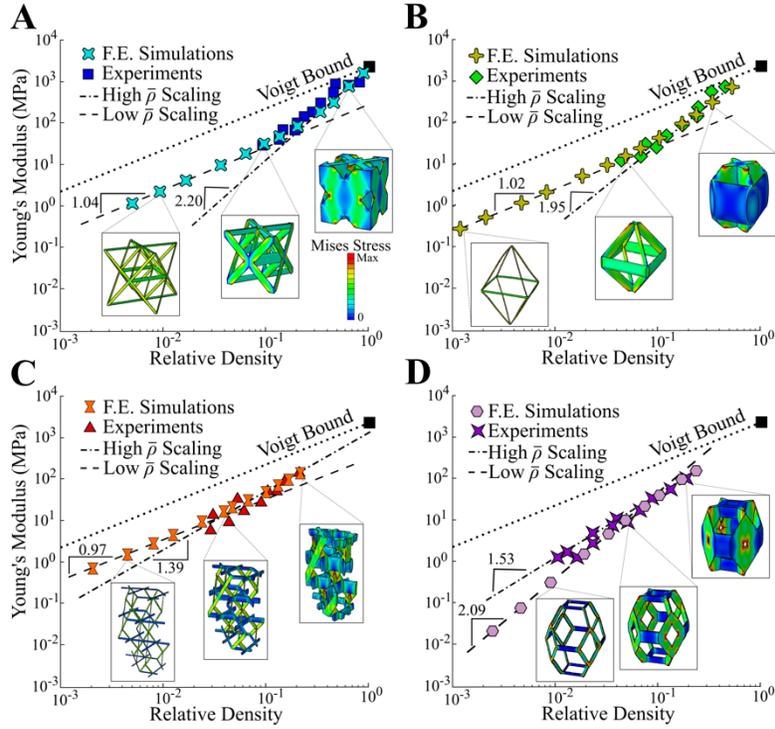
Figure 3: Solid-Beam Nanolattices FE and Experimental Young's Modulus v. Relative Density
Illustration of the comparison between FE and experimental results for A) octet-truss, B) octahedron, C) 3D Kagome, and D) tetrakaidecahedron lattices. The plots demonstrate the transition to the theoretical scaling relations at low density, as well as the agreement between experimental and FE results at low density. Insets show the stress distribution in the compressed lattices.
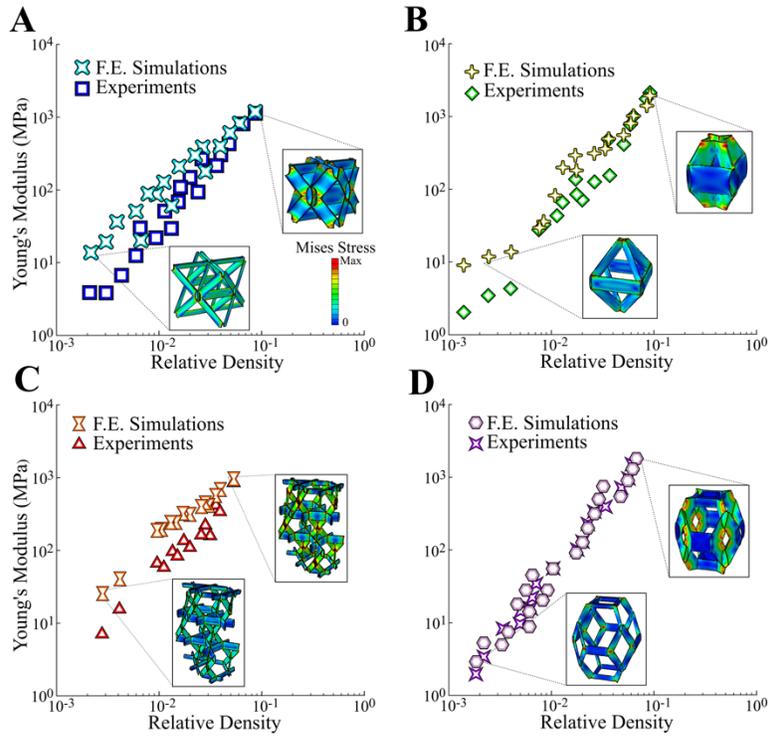
Figure 4: Hollow-Beam Nanolattices FE and Experimental Young's Modulus v. Relative Density
Illustration of the comparison between FE and experimental results for A) octet-truss, B) octahedron, C) 3D Kagome, and D) tetrakaidecahedron lattices, showing convincing agreement between experimental and FE results across the range of structural parameters tested experimentally. Insets show the stress distribution in the compressed lattices.
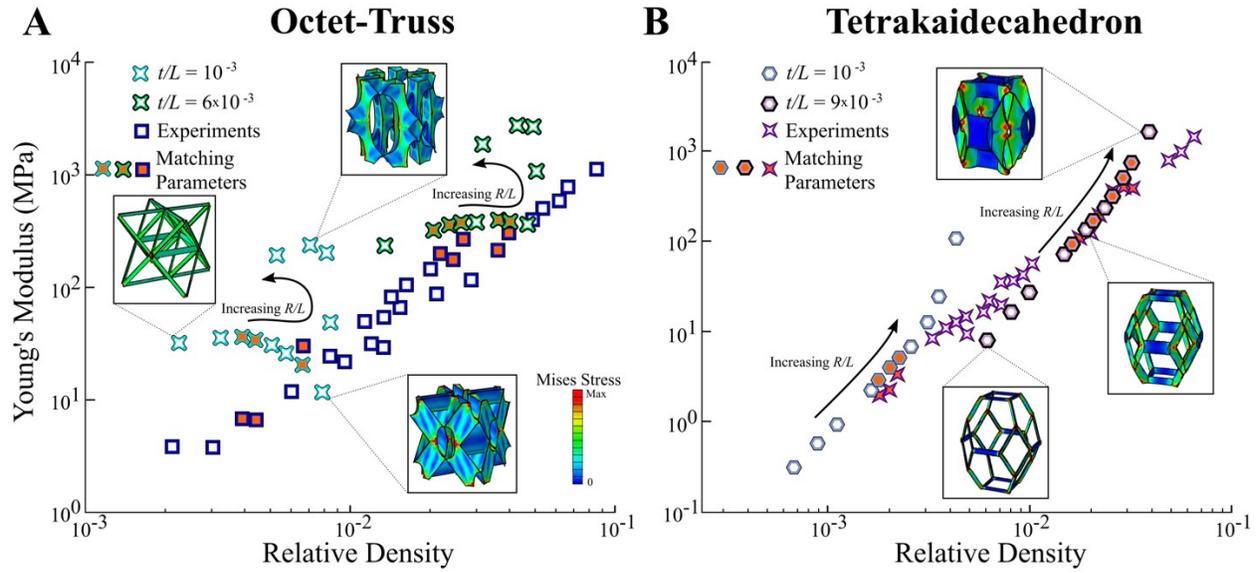
Figure 5: Hollow-Beam Octet-truss and Tetrakaidecahedron Nanolattice Simulation Results
Comparison of the stiffness data of A) octet-truss and B) tetrakaidecahedron lattices obtained from experiments and from finite element simulations. Two t/L values were studied for each geometry over a wide range of R/L values. Simulation and experimental data points with matching R/L and t/L values are filled with orange.

Material	Topology	B	m	C	n
Polymer	Octet-truss	0.82	1.77	1.31	1.88
	Cuboctahedron	1.09	1.83	1.59	1.92
	3D Kagome	0.43	1.41	0.97	1.68
	Tetrakaidecahedron	0.57	1.60	0.84	1.63
Al_2O_3	Octet-truss	0.39	1.63	1.14	1.71
	Cuboctahedron	0.52	1.69	0.82	1.64
	3D Kagome	0.26	1.46	0.44	1.45
	Tetrakaidecahedron	0.95	1.73	0.67	1.55

Table 1: *Experimentally derived scaling constants (m and n) and the proportionality constants (B and C) of the stiffness and strength scaling relationships respectively for each topology and each material system tested.*